

# Phase diagram of ferroelastic systems in the presence of disorder: Analytical model and experimental verification

R. Vasseur,<sup>1,2,3</sup> D. Xue,<sup>4</sup> Y. Zhou,<sup>4</sup> W. Ettoumi,<sup>5</sup> X. Ding,<sup>1,4,\*</sup> X. Ren,<sup>4,6</sup> and T. Lookman<sup>1,†</sup>

<sup>1</sup>*Theoretical Division and Center for Nonlinear Studies, Los Alamos National Laboratory, Los Alamos, New Mexico 87545, USA*

<sup>2</sup>*Institut de Physique Théorique, CEA Saclay, 91191 Gif Sur Yvette, France*

<sup>3</sup>*LPTENS, 24 rue Lhomond, 75231 Paris, France*

<sup>4</sup>*Multi-disciplinary Materials Research Center, Frontier Institute of Science and Technology, State Key Laboratory for Mechanical Behavior of Materials, Xi'an Jiaotong University, Xi'an 710049, China*

<sup>5</sup>*Laboratoire de Physique des Plasmas, CNRS–Ecole Polytechnique, 91128 Palaiseau cedex, France*

<sup>6</sup>*Ferroic Physics Group, National Institute for Materials Science, Tsukuba, 305-0047, Ibaraki, Japan*

(Received 21 December 2011; published 5 November 2012)

There is little consensus on the nature of the glass state and its relationship to other strain states in ferroelastic materials which show the shape memory effect and superelasticity. We provide a thermodynamic interpretation of the known strain states, including precursory tweed and strain-glass phases, by mapping the problem onto a spin model and analytically obtaining the phase diagram using real-space renormalization group methods. We further predict a spontaneous transition from the glass state to the ordered martensite phase. We verify this prediction by mapping out the experimental phase diagram for the ternary ferroelastic alloy  $\text{Ti}_{50}(\text{Pd}_{50-x}\text{Cr}_x)$  and demonstrate the emergence of the spontaneous transition. Our work thus provides a consistent framework in which to understand the various experimental and theoretical studies on the glassy behavior associated with ferroelastic materials.

DOI: [10.1103/PhysRevB.86.184103](https://doi.org/10.1103/PhysRevB.86.184103)

PACS number(s): 64.70.Nd, 61.43.Fs, 75.50.Lk, 81.30.Kf

## I. INTRODUCTION

Ferroelastic materials undergo first-order transitions that are characterized by a lattice strain or shuffle, and transform from a high-temperature strain-disordered paraelastic state (austenite) to a low-temperature strain-ordered ferroelastic state (martensite) where long-range elastic interactions are important. It is known that the thermodynamics of such phase transitions is strongly influenced by the presence of disorder.<sup>1–7</sup> In particular, statistical compositional fluctuations play a fundamental role in bringing about a precursory strain state known as tweed. This is a cross-hatched pattern observed well above the martensitic-transformation start temperature.<sup>8–10</sup> Recent experiments on ferroelastic alloys have shown that by introducing disorder via doping point defects or compositional variations beyond a critical value, an abnormal glasslike state, which is a frozen state of local strain order, can be generated below a transition temperature.<sup>11–15</sup> This glass phase was initially observed in Ni-rich  $\text{Ti}_{50-x}\text{Ni}_{50+x}$  where the austenitic  $B2$  parent structure appeared to persist to 0 K above a compositional threshold  $x > 1.3$ , below which it transformed to a martensitic  $B19'$  phase.<sup>11</sup> This so-called “strain glass” is of interest not only from a theoretical point of view; it has been shown to display superelasticity and shape memory effects, which are typically seen in austenitic and martensitic states.<sup>15</sup>

Experiments and theory have so far provided little understanding of the nature of the glassy behavior in ferroelastic materials and its relationship to other strain states. For example, the tweed state has been the subject of a number of theoretical studies and has variously been interpreted as a “glass” phase.<sup>9,10</sup> Although recent experiments distinguish strain glass from tweed,<sup>12</sup> the claims are largely based on diagnostics that monitor certain static and dynamic aspects of the materials;

these include the broken ergodicity of static properties [e.g., the strain measured by zero-field (ZFC) and field cooling (FC)], or frequency dispersion of dynamic properties.<sup>14</sup> However, nonglassy phases, such as polytwins in martensite or nanostructured ferromagnetics (e.g., FeReCr), also show similar nonergodic static behavior and frequency dispersion.<sup>16,17</sup> In addition, although numerical simulations based on continuum Landau descriptions in the presence of disorder<sup>13</sup> can reproduce some form of the experimental results,<sup>11–15</sup> such solutions are also based on similar empirical diagnostics and tend not to be predictive. Therefore, there is a need for a predictive approach using analytical techniques that would allow the various ordered and disordered ferroelastic states to be distinguished and which can be experimentally verified.

In this paper, we provide a thermodynamic interpretation of the known strain states in a ferroelastic system, including austenite, martensite, tweed, and strain glass. After mapping the problem onto a spin model, we use real-space renormalization group (RG) methods to analytically calculate thermodynamic phases in terms of RG attractive fixed points. The RG approach progressively integrates out microscopic degrees of freedom so that the attractive basins characterize the physics at large scales. The values of the interaction strength and strength of disorder uniquely characterize the different phases, including the frustrated glassy state, thereby allowing the phase diagram in terms of temperature and disorder to be determined. We thus theoretically determine the phase diagram of a model ferroelastic, and the phase diagram predicts a spontaneous transition from strain glass to martensite if the strength of disorder in the system has intermediate values. This latter aspect was apparently not recognized previously, although it has recently been speculated that the spontaneous transition occurs.<sup>18</sup> We verify these predictions by mapping out the experimental diagram for

a ternary ferroelastic  $\text{Ti}_{50}(\text{Pd}_{50-x}\text{Cr}_x)$  alloy (where  $x$  is the atomic concentration of Cr) and examining its consequences. Moreover, our calculations show that the tweed phase can be interpreted as a thermodynamic equilibrium phase. Our model thus provides a unified, consistent framework in which to understand the various experimental and theoretical studies on the glassy behavior associated with ferroelastic materials. Moreover, we find that the long-range elastic interaction or the precise form of the disorder is not crucial to describing the phase diagram. These ideas are well recognized for spin glasses but are not as well known within the strain-glass community.

The plan of our paper is as follows. In the next section, we review how effective spin models can be deduced from Ginzburg-Landau (GL) functionals, and we discuss the various means to include quenched disorder in the model. The third section is devoted to the calculation of the analytical phase diagram from our model in the presence of disorder. We explain how a real-space RG procedure can be implemented and we present several approaches and approximations to solve the resulting equations. The results are compared to Monte Carlo simulations and we provide a discussion of the relevance of simplified numerical algorithms—be it a one-spin-flip Monte Carlo or the steepest-descent method for the continuum GL model—for these types of problems. The role of the long-range interactions is also discussed in relation to previous work. Section IV contains our experimental results on  $\text{Ti}_{50}(\text{Pd}_{50-x}\text{Cr}_x)$  alloys. We measure the transformation behavior of the alloys by means of dynamical mechanical analysis (DMA) and the electric resistivity. *In situ* synchrotron x-ray and transmission electron microscopy (TEM) were employed to detect the predicted spontaneous phase transformation. Our experiments lead to a phase diagram that is very similar to the one we establish analytically. Finally, we discuss our results in the broader context of ferroelastic transitions in general and the possible generalizations of our theoretical work to more complex transitions.

## II. PSEUDOSPIN MODEL AND QUENCHED IMPURITIES

Our approach is to use a model that captures the salient physics and microstructure associated with ferroelastic transformations. We will use a pseudospin model derived from a continuum formulation based on a Landau potential and strain compatibility forces.<sup>19,20</sup> The addition of quenched disorder then permits studies of the model using the tools of statistical mechanics. We review in this section the crucial steps in the derivation of such spin models starting from standard Ginzburg-Landau free-energy functionals. We then discuss how the effect of impurities in the original GL theories can be taken into account in spin models.

### A. Spin model

The idea of using a spin model for ferroelastic transitions was introduced in Ref. 19. This idea was later generalized to many other transitions and shown to capture the salient physics of continuum GL models.<sup>20</sup> For simplicity, we will study here the two-dimensional (2D) square-to-rectangle (SR) transformation driven by the deviatoric strain  $e_2 = \frac{1}{\sqrt{2}}(\epsilon_{11} - \epsilon_{22})$ ,

where  $\epsilon_{\mu\nu}$  are components of the strain tensor  $\epsilon_{\mu\nu} = \frac{1}{2}(\frac{\partial u_\mu}{\partial r_\nu} + \frac{\partial u_\nu}{\partial r_\mu})$  defined in terms of displacements  $u$ . The generalization to more complicated—and more realistic—transitions will be discussed in Sec. V. The Landau free energy of the system is  $F_{\text{GL}}[e_2] = E_0 \int d^2r [f_L + f_G + f_{LR}]$ , where the local free energy for the first-order transition is  $f_L = (\tau - 1)e_2^2 + e_2^2(e_2^2 - 1)^2$ , the gradient term  $f_G = \xi^2 |\nabla e_2|^2$  accounts for the cost of creating interfaces between different variants, and  $f_{LR} = \frac{A_1}{2} \int d^2r' e_2(\vec{r}) U(\vec{r} - \vec{r}') e_2(\vec{r}')$  is the elastic long-range force. The scaled temperature  $\tau = \frac{T - T_c}{T_{\text{eq}} - T_c}$  is expressed in terms of the transition temperature  $T_{\text{eq}}$  and  $T_c$  is the temperature of the austenite stability limit. The long-range term comes from the so-called compatibility equation  $\vec{\nabla} \times (\vec{\nabla} \times \epsilon)^T = 0$  on the strain tensor  $\epsilon$ , that ensures that the displacement field is single valued. This leads to the anisotropic kernel  $U(\vec{r} - \vec{r}')$ , which reads in Fourier space

$$\hat{U}(\vec{k}) = \frac{(k_x^2 - k_y^2)^2}{k^4 + 8A_1 k_x^2 k_y^2 / A_3} v(\vec{k}). \quad (1)$$

The factor  $v(\vec{k}) = 1 - \delta_{k,0}$  ensures that this long-range term vanishes for a uniform strain field. In all that follows, the ratio  $A_1/A_3 = \frac{1}{2}$  will be kept constant. Transforming back into real space, we roughly have  $U \simeq \frac{\cos 4\theta}{r^2}$ .

The strain  $e_2$  is the order parameter for this transition. The Landau term  $f_L = (\tau - 1)e_2^2 + e_2^2(e_2^2 - 1)^2$  ensures that the system undergoes a first-order phase transition at  $\tau = 1$ . When  $\tau < 4/3$ , this term has three minima, which correspond to phases called austenite ( $e_2 = 0$ ) and martensite [ $e_2 = \pm \varepsilon(\tau)$ ], where  $\varepsilon(\tau) = [\frac{2}{3}(1 + \sqrt{1 - \frac{3\tau}{4}})]^{1/2}$ . For  $1 < \tau < 4/3$ , the martensite is a metastable state. To obtain nonuniform textures, one minimizes the GL functional  $F_{\text{GL}}[e_2]$  as usual. Note that at this stage the GL continuum model is in itself a mean-field description of the microscopic problem, and as such it does not contain any information about fluctuations around the mean-field solution given by the minimization of  $F_{\text{GL}}[e_2]$ . An alternative point of view is to consider a formal partition function  $\mathcal{Z} = \int \mathcal{D}[e_2] \exp(-\beta F[e_2])$ , where the strain configurations are summed over with a weight given by the usual Boltzmann weight. The Landau (or mean-field) approximation is then nothing but a saddle-point calculation of this functional integral. One can simplify the calculation of  $\mathcal{Z}$  by retaining only the strain minima given by the Landau part of  $F$ , transforming then  $e_2$  into a discrete variable that we rewrite as  $e_2(\vec{r}) = \varepsilon(\tau) S(\vec{r})$  with the pseudospin  $S(\vec{r}) = 0, \pm 1$ . This is the main point of the pseudospin approximation; instead of keeping only one configuration which minimizes the full GL functional  $F_{\text{GL}}[e_2]$ , we retain in the partition function all the configurations that minimize the local Landau term  $f_L = (\tau - 1)e_2^2 + e_2^2(e_2^2 - 1)^2$ . Within this approximation, the partition function reads  $\mathcal{Z} \simeq \sum_{\{S\}} \exp(-\beta H)$ , where the Hamiltonian  $H$  is obtained from the continuum theory as  $H = F_{\text{GL}}[e_2(\vec{r})] \rightarrow \varepsilon(\tau) S(\vec{r})$ . After a proper discretization,<sup>19,20</sup> it reads

$$\beta H = -J(\tau) \sum_{\langle i,j \rangle} S_i S_j + \Delta(\tau) \sum_i S_i^2 + \frac{\beta A_1}{2} \sum_{ij} S_i U_{ij} S_j, \quad (2)$$

where  $\Delta(\tau) = D_0(\tau)/2[g_L(\tau) + 4\xi^2]$  and  $J(\tau) = D_0(\tau)\xi^2$ , with  $D_0 = 2\beta E_0 \varepsilon(\tau)^2$  and  $g_L = (\tau - 1) + [\varepsilon^2(\tau) - 1]^2$ . The states  $S_i = \pm 1$  correspond to the two rectangular variants while  $S_i = 0$  represents the square austenite. Note that this spin model makes sense only for  $\tau \leq 4/3$ , as for  $\tau > 4/3$  only the state  $S = 0$  is allowed. We have therefore mapped our continuum GL theory onto a lattice spin-1 model with Hamiltonian (2). This Hamiltonian with  $A_1 = 0$  is known in the spin literature as the Blume-Capel model<sup>21</sup> and it reproduces all the well-known features of the transition;<sup>20</sup> in particular, it has a first-order transition around  $\tau \simeq 1$ .

There are several points that are worth mentioning at this stage. It is usual to deduce GL theories from lattice models, not the other way around. The reason for this is that GL theories are easier to deal with and contain interesting coarse-grained, mean-field information about the initial microscopic model. In our case, we chose to start from a simplified GL theory to map onto a spin-1 statistical model that may seem harder to handle. On the other hand, spin models will turn out to be very convenient when introducing quenched disorder as connections to the usual spin-glass models can then be made.<sup>8,22</sup> It is also important to realize that when progressing from mean-field GL theory to a classical spin model we have actually put in additional information about thermal fluctuations, as the former *a priori* does not contain any information about fluctuations around the mean-field solution. The Hamiltonian (2) is an *effective* model, with temperature-dependent coefficients and is *not* an accurate microscopic description of the phenomenon that we are studying. The additional information contained in the effective Hamiltonian (2) is somewhat arbitrary and other choices of reasonable Hamiltonian would be possible. For example, one could as well have introduced two different temperatures, the physical temperature  $T$  that would appear in  $\tau$ , and another more artificial temperature  $T_e$  that would appear in the Boltzmann factor  $\exp(-H/T_e)$ . As was suggested in Ref. 8, one can then also let  $T_e = 0$  so that one would need to minimize  $H$  in order to obtain statistical properties. We chose to introduce somewhat artificially thermal fluctuations by taking  $T = T_e$ , a point of view completely analogous to what is usually done with the well-known  $\phi^4$  theory. This is a crucial point when dealing with such effective spin models.

### B. Spin model with quenched disorder

Now that we have seen how to model ferroelasticity using spin models, we consider the influence of impurities in the model. Our aim is to understand how quenched impurities affect the phase diagram of ferroelastic materials. This is usually done phenomenologically in Landau theory<sup>13</sup> by introducing a random field or by introducing randomness in the transition temperature  $T_c$  with nonzero spatial correlations.<sup>23,24</sup> In this paper, we follow the idea that one need not worry about the precise microscopic form of the disorder induced by impurities as one expects the effect of quench disorder in the interactions of the model to yield somewhat universal features. Recall that our spin model is an effective model, so the results we are after are generic features of the phase diagram, such as its topology, rather than an accurate, quantitative description to be compared directly with experiments. Note that this train of

thought is very similar to what was done in spin-glass theory for the usual ferromagnets (see, e.g., Refs. 25–27). The point is then to start from the pure (disorder-free) Hamiltonian (2) and to take the nearest-neighbor couplings to be quenched-independent random variables  $J_{ij}$ , drawn from the distribution  $\mathcal{P}(J_{ij})$ , with mean  $J(\tau)$  and with variance  $\sigma_J$ . As we will see later, the precise form of this distribution is irrelevant to the global topology of the phase diagram. This is a strong argument in favor of the “universality” discussed previously. We believe that this way of introducing disorder tends to be more satisfying than the very specific, sometimes fine-tuned, methods usually used in the literature. The parameter  $\sigma_J$  can be thought of as a measure of the quenched disorder in the system; in particular, for  $\sigma_J = 0$  we recover a pure system. For future reference, we give the explicit form of our disordered Hamiltonian:

$$\beta H = - \sum_{\langle i,j \rangle} J_{ij}(\tau) S_i S_j + \Delta(\tau) \sum_i S_i^2 + \frac{\beta A_1}{2} \sum_{ij} S_i U_{ij} S_j, \quad (3)$$

where the couplings  $J_{ij}$  are quenched variables drawn from the distribution  $\mathcal{P}(J_{ij})$ . In this paper we will use two different types of distribution:

$$\mathcal{P}(J_{ij}) = \frac{1}{2} \delta(J_{ij} - J_1) + \frac{1}{2} \delta(J_{ij} - J_2), \quad (4a)$$

$$\mathcal{P}(J_{ij}) = \frac{1}{\sqrt{2\pi}\sigma_J} \exp\left(-\frac{[J_{ij} - J(\tau)]^2}{2\sigma_J^2}\right), \quad (4b)$$

with  $J_1 = J(\tau) + \sigma_J$  and  $J_2 = J(\tau) - \sigma_J$ . In the following, the distribution (4a) will be referred to as “bimodal” whereas we will denote (4b) as Gaussian. These equations define the model we will attempt to solve in the next section.

## III. PHASE DIAGRAM

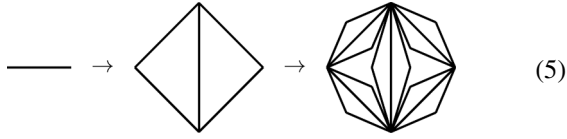
We now consider how real-space renormalization group can be used to compute the full phase diagram of the spin model (3). We also present preliminary Monte Carlo results and discuss their relationship to the phase diagram of the model.

### A. Real-space renormalization group for the pure model

Our goal in this section is to obtain an analytical phase diagram of the model defined by Eq. (2) in the limit  $A_1 = 0$ . From now on we will take only the limit of vanishing long-range interactions  $A_1 = 0$  as we do not believe they are important to understand the phase diagram of ferroelastic materials. We will return to this later. There are several ways to deal with a Hamiltonian such as (2); an obvious straightforward method would be to perform a mean-field approximation. This yields (see, e.g., Ref. 20 for a description in the context of martensitic transitions) a first-order phase transition at  $\tau \simeq 1$  between a martensite phase with  $m = \langle S \rangle \neq 0$  and a high-temperature austenite phase characterized by  $m = 0$ . Here we choose a different, usually more reliable method: the real-space renormalization group. Its application to our pure spin-1 model goes back to Ref. 28 and is of course well known. We review here some of the essential elements before proceeding to the case of disorder.

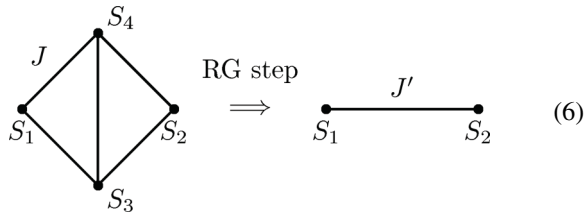


The idea is to approximate the square lattice by a hierarchical lattice, obtained by iterating the construction scheme



Several other choices of hierarchical lattices to approximate the square lattice are possible; however, the one we chose is known to be a very good approximation in the case of spin-1 models (see, e.g., Ref. 29). We define our spin model on such a lattice by the Hamiltonian  $\beta H = -J \sum_{\langle i,j \rangle} S_i S_j + \frac{\Delta}{4} \sum_{\langle i,j \rangle} (S_i^2 + S_j^2)$ . Note that we expressed the crystal-field term  $\Delta$  as a sum over the links instead of a sum over sites in order to take into account the fact that the coordination number of the sites in the lattice (5) is not constant. It is well known that such precautions are needed when dealing with the renormalization of local field terms such as  $-h \sum S_i$  or specifically here  $\Delta \sum S_i^2$ . This corresponds to assigning weights to the sites in the crystal-field interaction term ( $\Delta$ ) according to their coordination numbers which in this lattice, unlike the square lattice, are not uniform. This inhomogeneity is necessary so that the square lattice is correctly approximated using a hierarchical lattice.

On such a lattice, the partition function can be computed exactly by summing progressively over the spins. The renormalization procedure consists in decimating spins according to the scheme



so that the renormalization process corresponds to inverting the arrows in Eq. (5). More formally, if one denotes by  $H_{1234}$  the Hamiltonian of the left-hand side of Eq. (6) and by  $H'_{12}$  its right-hand side, one has

$$\exp[-\beta H'_{12}] = \text{Tr} \exp[-\beta H_{1234}], \quad (7)$$

where Tr amounts to a partial summation performed on spins  $S_3$  and  $S_4$ . This equation then gives the relationship between  $H_{1234}$  and the renormalized Hamiltonian  $H'_{12}$ , so that one can draw the evolution of the coupling parameters by repeating this decimation procedure. It is not hard to see that this transformation is exact if and only if one introduces an additional coupling  $-K \sum_{\langle i,j \rangle} S_i^2 S_j^2$  that is generated upon renormalization. Although this biquadratic interaction is absent in our original model, it is generated by the RG procedure, and must be taken into account to follow the exact RG flow. In our case, the elementary Hamiltonian  $\mathcal{H}_{1234}$  reads  $\beta H_{1234} = -\sum_{\langle i,j \rangle} [J S_i S_j + K S_i^2 S_j^2] + \frac{1}{4} \Delta \sum_{\langle i,j \rangle} [S_i^2 + S_j^2]$ , where the sum are performed over the links ( $\langle 13 \rangle, \langle 14 \rangle, \langle 42 \rangle, \langle 32 \rangle, \langle 34 \rangle$ ) in Eq. (6). It is worth emphasizing again that the additional coupling term  $-K \sum_{\langle i,j \rangle} S_i^2 S_j^2$  must be introduced in the Hamiltonian, otherwise there is no analytical solution to be found for Eq. (7). The renormalized Hamiltonian  $\mathcal{H}'_{12}$  then reads  $\beta H'_{12} = -J' S_1 S_2 - K' S_1^2 S_2^2 + \frac{\Delta'}{4} (S_1^2 + S_2^2) + C'$ , where  $C'$  becomes

a simple multiplying constant  $\exp(-C')$  that contributes to the renormalization of the free energy, irrelevant for our purposes.

It is straightforward to solve Eq. (7) for all  $S_1, S_2$ . This yields a nonlinear map  $(J', \Delta', K') = \mathcal{R}[J, \Delta, K]$  that gives the exact renormalized couplings of the effective Hamiltonian  $H'$  in terms of the initial ones. By iterating this map, one can obtain the effective Hamiltonian describing the physics of the system at large scale, where the microscopic degrees of freedom of the system have been summed over. Basins of attraction of this map correspond to thermodynamical phases, characterized by attractive fixed points. For example, the martensite phase (ferromagnetic phase in the spin language) has  $J^* = +\infty$  and  $\Delta^* = -\infty$ , so at large scales the effective Hamiltonian describing the system forces the spin to be in the  $S = \pm 1$  states, with a strong correlation between nearest neighbors. Meanwhile, austenite can be described by the attractive fixed point  $J^* = 0$  and  $\Delta^* = \infty$  so it corresponds to a disordered phase that favors  $S = 0$ . To obtain the phase diagram of our spin model (2) for  $A_1 = 0$ , we simply iterate the map  $\mathcal{R}$  starting from the initial point  $(J, \Delta, K) = (J(\tau), \Delta(\tau), 0)$ . We find that the system flows to the martensite fixed point for  $\tau \lesssim 0.96$  and to the austenite fixed point for  $\tau \gtrsim 0.96$ . Moreover, the study of the largest eigenvalue of the linearized renormalization group matrix around the transition at  $\tau \simeq 0.96$  can be used to prove that the transition is of first order,<sup>28,29</sup> as expected.

## B. Real-space renormalization group with disorder

The idea of using spin-glass models to describe disordered ferroelastic materials originates from Refs. 8 and 22. The mean-field replica approach of this model<sup>22,30</sup> yields a strain-glass phase but also several unwanted features that are contrary to both experiments and Monte Carlo simulations. The absence of a tweed precursor is an example. We use here a different approach relying on real-space RG which we believe is simpler and usually more reliable. Although our starting point is the same Hamiltonian (3), we will see in this paper that the RG provides interesting results that can be tested experimentally.

The implementation of the RG procedure for disordered systems is very similar to the pure case in Sec. III A. The real-space RG in disordered systems still relies on a decimation procedure to progressively sum over the spin variables, integrating out the microscopic degrees of freedom (see, e.g., Refs. 28, 29, and 31). After each summation step, the effective Hamiltonian describing the remaining degrees of freedom is assumed to be the same as the original one but with renormalized coupling coefficients. This turns out to be exact for the hierarchical lattice (5). The only difference is that for disordered systems the RG allows us to follow the probability distribution of the couplings upon the renormalization procedure instead of the couplings themselves. In order to do so, the main point is to obtain the RG equations in the case of a completely inhomogeneous system. Even though the initial Hamiltonian (3) (with  $A_1 = 0$ ) has pure  $K = 0$  and  $\Delta$  interactions, the RG flow will lead to randomness in all couplings, so one has to consider the more general Hamiltonian  $\beta H = -\sum_{\langle i,j \rangle} [J_{ij} S_i S_j + K_{ij} S_i^2 S_j^2 - \frac{\Delta_{ij}}{4} (S_i^2 + S_j^2) - \frac{\Delta_{ij}^\dagger}{4} (S_i^2 - S_j^2)]$ . The initial condition for the RG flow is the Hamiltonian (3) with  $A_1 = 0$ , so that before renormalization,

$K_{ij} = 0$ ,  $\Delta_{ij} = \Delta(\tau)$ , and  $\Delta_{ij}^\dagger = 0$ . Note that we once again considered the crystal-field term as existing on the edges of the lattice and not on the sites. This should be reminiscent of our treatment of the pure case in Sec. III A. The solution of Eq. (7) in this case yields a map  $\mathcal{R}$  that gives the renormalized couplings  $(J'_{12}, K'_{12}, \Delta'_{12}, \Delta'_{12}^\dagger)$  in terms of the original ones  $(J_{14}, J_{13}, \dots, K_{14}, K_{13}, \dots, \Delta_{14}, \Delta_{13}, \dots, \Delta_{14}^\dagger, \Delta_{13}^\dagger, \dots)$ . One then analyzes the evolution of the joint probability distribution  $\mathcal{P}(J_{ij}, K_{ij}, \Delta_{ij}, \Delta_{ij}^\dagger)$  upon renormalization, starting from the initial distributions  $\mathcal{P}(\Delta_{ij}) = \delta(\Delta_{ij} - \Delta(\tau))$ ,  $\mathcal{P}(\Delta_{ij}^\dagger) = \delta(\Delta_{ij}^\dagger)$ ,  $\mathcal{P}(K_{ij}) = \delta(K_{ij})$ , and  $\mathcal{P}(J_{ij})$  given by either (4a) or (4b). Let us now be slightly more explicit. Let  $\mathbf{K}_{ij} = (J_{ij}, K_{ij}, \Delta_{ij}, \Delta_{ij}^\dagger)$  denote the four couplings existing on the link  $(ij)$ . The RG maps  $\mathbf{K}'_{ij} = \mathcal{R}[\{\mathbf{K}_{ij}\}]$  then gives the four renormalized couplings  $\mathbf{K}'_{ij} = (J'_{12}, K'_{12}, \Delta'_{12}, \Delta'_{12}^\dagger)$  as a function of the 20 initial ones  $\{\mathbf{K}_{ij}\} = (\mathbf{K}_{13}, \mathbf{K}_{14}, \mathbf{K}_{34}, \mathbf{K}_{23}, \mathbf{K}_{42})$ , where we used the labeling of Eq. (6). The RG recursion relation for the joint distribution  $\mathcal{P}(\mathbf{K}_{ij}) = \mathcal{P}(J_{ij}, K_{ij}, \Delta_{ij}, \Delta_{ij}^\dagger)$  then reads

$$\mathcal{P}'(\mathbf{K}'_{ij}) = \int \left[ \prod_{ij} d\mathbf{K}_{ij} \mathcal{P}(\mathbf{K}_{ij}) \right] \delta(\mathbf{K}'_{ij} - \mathcal{R}[\{\mathbf{K}_{ij}\}]), \quad (8)$$

where the product is over the five links of Eq. (6), so there are 20 integrations to be performed at each RG step. We emphasize again that even though one starts from pure  $K$  and  $\Delta$  couplings, randomness in these parameters will be generated by the RG procedure. Similarly, even if one starts from a bimodal Gaussian distribution for  $\mathcal{P}(J_{ij})$ , the resulting distribution obtained after several renormalization steps could in principle be much more complicated.

### C. Basins of attraction and thermodynamical phases

Before solving explicitly Eq. (8), let us discuss how the phases are characterized within this formalism. The RG distribution  $\mathcal{P}(J_{ij}, K_{ij}, \Delta_{ij}, \Delta_{ij}^\dagger)$  will typically flow to attractive fixed points that will characterize thermodynamical phases. In principle, one would need an infinite number of parameters to characterize RG-invariant distributions  $\mathcal{P}^*(J_{ij}, K_{ij}, \Delta_{ij}, \Delta_{ij}^\dagger)$ . However, for our purposes it turns out that the thermodynamic phases can be obtained as RG basins of attraction characterized only by the values of  $\Delta^*$  and  $(J^*, \sigma_J^*)$  at the fixed point. Here  $\Delta^*$  and  $J^*$  are the mean values of  $J$  and  $\Delta$  at the fixed point, while  $\sigma_J^*$  is the standard deviation of  $J$ .

The martensite (ferroelastic) phase corresponds to the usual ordered ferromagnetic phase ( $J^* = \infty, \Delta^* = -\infty, \sigma_J^*/J^* = 0$ ). In terms of order parameters (OPs) used in mean-field theory and replica calculations (see, e.g., Ref. 22), this phase is characterized by a nonzero magnetization  $m = \overline{\langle S_i \rangle} \neq 0$ , where the overbar represents an average over the disorder and the angular brackets an average with respect to Boltzmann weights. We find two paraelastic disordered phases with  $J^* = 0$ ,  $\sigma_J^* = 0$ , and  $\Delta^* = \pm\infty$ . The case  $\Delta^* = \infty$  corresponds to the austenite case as it favors  $S = 0$ , whereas the case  $\Delta^* = -\infty$  is interpreted as a disordered phase of martensite clusters which we identify as the tweed phase. The OP that allows us to distinguish between the two phases is

TABLE I. Characterization of the different thermodynamic phases in terms of the calculated renormalization group fixed points. The austenite and tweed phases are clearly separated because one fixed point has the value  $\Delta^* = +\infty$  (so the state  $S = 0$  is favored) whereas the other has  $\Delta^* = -\infty$ . We also show the corresponding OP values  $m = \overline{\langle S_i \rangle}$ ,  $p = \overline{\langle S_i^2 \rangle}$ , and  $q = \overline{\langle S_i \rangle^2}$  for the phases as characterized in mean-field and replica theory.

Phase	OP characterization	RG fixed point
Austenite	$m = q = 0$ , $p$ small	$\Delta^* = +\infty$ , $J^* = 0$ , $\sigma_J^* = 0$
Martensite	$m \neq 0$ , $p \neq 0$ , $q \neq 0$	$\Delta^* = -\infty$ , $J^* = \infty$ , $\frac{\sigma_J^*}{J^*} = 0$
Tweed	$m = q = 0$ , $p$ large	$\Delta^* = -\infty$ , $J^* = 0$ , $\sigma_J^* = 0$
Strain glass	$m = 0$ , $p \neq 0$ , $q \neq 0$	$\Delta^* = -\infty$ , $J^* = 0$ , $\sigma_J^* = \infty$

the “martensite volume fraction”  $p = \overline{\langle S_i^2 \rangle}$ . We also remark that the tweed precursor we find is ergodic and nonglassy, consistent with results of recent experiments.<sup>32</sup> This is to be compared with the hypothesis of Refs. 9 and 10 that interpreted tweed as a glassy phase. Our model results are that tweed is a thermodynamic phase, rather than a metastable precursor. Note also that this tweed phase is not captured by a mean-field replica-symmetric analysis of our 2D model.<sup>22</sup> The last phase that we encounter corresponds to a spin or strain glass with infinite randomness ( $\sigma_J^* = \infty$ ) and ( $J^* = 0$ ,  $\Delta^* = \infty$ ). The effective Hamiltonian describing the system at large scales has features in which variants  $S = \pm 1$  are favored (because  $\Delta^* = \infty$ ), and the values  $J^* = 0$  and  $\sigma_J^* = \infty$  imply random infinite couplings on each bond, thus denoting frustration. This phase is also characterized by the Edwards-Anderson order parameter  $q = \overline{\langle S_i \rangle^2}$  which in the replica language corresponds to the overlap between two replicas  $q = \overline{\langle S_i^1 S_i^2 \rangle}$  of the system.<sup>25</sup> The characterization in terms of RG fixed points or OPs of these four thermodynamic phases is gathered in Table I.

### D. Analytical phase diagram

#### 1. Numerical resolution

We now discuss how one can solve (8). An obvious method would be to sample numerically the joint distribution  $\mathcal{P}(J_{ij}, K_{ij}, \Delta_{ij}, \Delta_{ij}^\dagger)$ . This allows one to solve explicitly Eq. (8) numerically. We used pools of 160 000 values to sample the distribution  $\mathcal{P}(J_{ij}, K_{ij}, \Delta_{ij}, \Delta_{ij}^\dagger)$ . The results are shown in Fig. 1 for both bimodal (4a) and Gaussian (4b) initial distributions. The parameters appropriate for our example are  $E_0 = 3$ ,  $\xi = 0.5$ ,  $T_{\text{eq}} = 1$ , and  $T_c = 0.9$ . Note that, strictly speaking, our spin model is not defined for  $\tau > 4/3$ , as the spin approximation yields only one state  $S = 0$  in that case. However, we can still think of this region as being in the austenite phase, as this is the only phase allowed by the spin approximation. One of the most striking features of these phase diagrams is the appearance of an intermediate tweed phase between the austenite and martensite phases as the disorder is turned on. This is consistent with what is known experimentally (see Sec. IV). Meanwhile, the phase diagram has the same topology for both types of disorder. This is a strong result in favor of the universality discussed in Sec. II A.

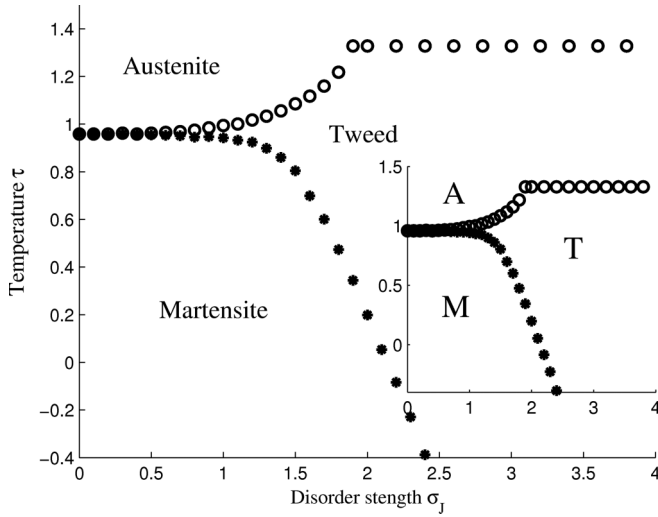


FIG. 1. Analytical phase diagrams from the exact numerical resolution of the RG equations on the hierarchical lattice. Main figure: the initial distribution of the disorder was taken to be bimodal. Inset: initial Gaussian distribution. Notice the absence of a spin- or strain-glass phase (see the text).

One notes the absence of the spin- or strain-glass phase, which is to be expected. Strictly speaking, the model (3) in two dimensions should not have a spin-glass phase at finite temperature.<sup>31</sup> To be more precise, the Hamiltonian (3) is believed to have a spin-glass lower critical dimension  $d_c$  lying somewhere between 2 and 3. This means that for  $d < d_c$  (low dimension), and in particular for  $d = 2$ , the spin-glass phase should be destroyed by thermal fluctuations. Meanwhile, it was recently proved<sup>31</sup> that the very same model (forgetting about the temperature dependence of the coefficients) has a spin-glass phase at finite temperature in 3D. (Note that the SR transition embedded in 3D—or in our spin model in 3D—corresponds to a slightly constrained tetragonal-to-orthorhombic transition.) Of course, a spin-glass phase can also be found within a mean-field or replica solution of the model,<sup>22</sup> as the mean field effectively corresponds to  $d = \infty$ . We expect this spin-glass phase to reappear on higher-dimensional hierarchical lattices.<sup>31</sup> Although one might think that the absence of a spin-glass phase in 2D could be of crucial importance experimentally, this is actually irrelevant to us, for the following reasons:

(a) Even though a spin-glass phase should not exist in 2D, we still expect kinetic features to make the system look “glassy.” This will be discussed in more detail in Sec. III E below. The point is that the distinction in experiments and numerics between a genuine spin-glass phase and a glassy kinematic behavior is actually a very subtle issue.

(b) As our spin model was derived from a mean-field Landau energy without thermal fluctuations, we are interested in generic (mean-field-like) features of our model. This is a consequence of the discussion at the end of Sec. II A. The spin-glass lower critical dimension is not a meaningful quantity in our case as our model was derived from a mean-field Landau energy in the first place. Therefore, the fact that the somewhat artificial fluctuations—introduced in going from the continuum GL theory to our spin model—may or may

not destroy the spin-glass phase is not relevant, as these fluctuations do not exist in the original Landau model. Our model is thus meaningful only in a mean-field-like context.

Therefore, one need not worry about this issue of the lower critical dimension here; it would be meaningful only if our spin model were a precise microscopic description of ferroelastics.

## 2. Projection approximation

Although the direct numerical resolution of Eq. (8) is the most straightforward way to proceed, it is also useful to have an approximate way of solving this system, thereby allowing one to perform the calculations analytically. A possibility to avoid this rather cumbersome numerical procedure is to make a further approximation in the case of bimodal disorder (4a). One can remark that rather than follow the full evolution of these distributions, one could enforce the renormalized distributions to be the same as the initial ones but with renormalized parameters. That is, we enforce the distribution of the  $J_{ij}$  couplings to remain bimodal upon renormalization, keeping  $K$  and  $\Delta$  constant. Although this approximation may appear too drastic, it is quite common in spin-glass-related problems and we will show in the following that it captures all the important features of the phase diagram of the model (3). Note that such an approximation typically yields results characteristic of higher-dimensional systems (see, e.g., Ref. 29 and references therein), and thus should alter the spin-glass lower critical dimension. As discussed previously, this is not important for our purposes. In the following, we will refer to this approximation as the “projection approximation,” as it indeed consists in projecting the renormalized distributions onto the initial ones.

Figure 2(a) shows the phase diagram in the plane  $(\tau, \sigma_J)$  obtained by iterating the RG map in the projection approximation case. In the absence of disorder ( $\sigma_J = 0$ ), we find a first-order phase transition between the austenite and martensite phases with  $\tau \simeq 1$ , as expected. As one increases the disorder, an intermediate tweed phase arises before it transforms into the low-temperature phase (either martensite or strain glass). For large enough disorder and low temperature, we find a spin-glass phase that we interpret as a strain glass. Interestingly, when the disorder of the system is in the intermediate regime ( $1.3 < \sigma_J < 2.3$  in our model), we find there should exist a spontaneous phase transition from strain glass to martensite; this is a prediction that was not obtained by previous numerical simulations<sup>13,19,23,24,33</sup> based on Landau theory. The existence of a spin-glass phase in this calculation is related to our projection approximation, which is known to produce results characteristic of higher-dimensional systems (it is therefore legitimate to think of this approximation as a kind of mean field). Note also that except for the spin-glass phase, the exact numerical resolutions of Fig. 1 and the projection approximation results of Fig. 2(a) are very much alike.

## E. Monte Carlo simulations and influence of long-range interactions

We also present some preliminary Monte Carlo (MC) simulations that tend to confirm our RG results. We first note that one has to be very careful when doing MC simulations on a disordered system; in particular, one has to use algorithms



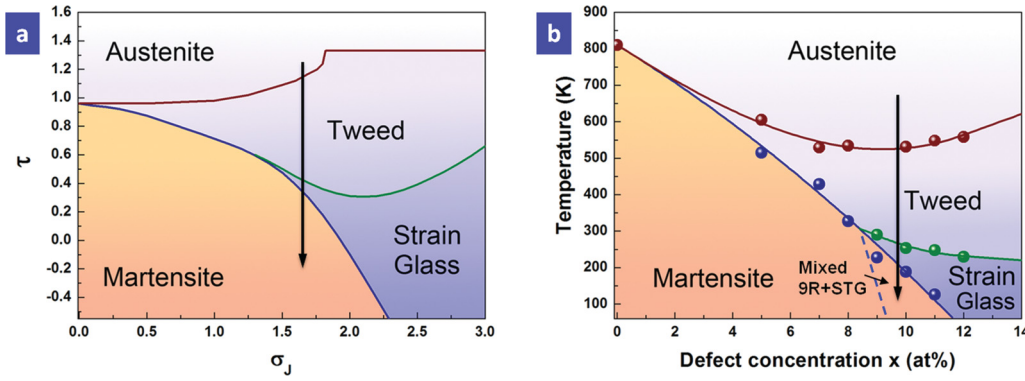


FIG. 2. (Color online) Comparison between theoretical and experimental phase diagrams. (a) Phase diagram in the temperature-disorder  $(\tau, \sigma_J)$  plane for our spin model, obtained within the RG projection approximation.  $\tau$  is the normalized temperature and  $\sigma_J$  characterizes the amount of quenched disorder in the system. (b) Experimental phase diagram of the ternary ferroelastic  $\text{Ti}_{50}(\text{Pd}_{50-x}\text{Cr}_x)$ . STG refers to strain glass. 9R is a new martensite phase formed, other than B19, if TiPd-based alloys are doped with certain defects. It is a martensite with long periodic stacking structure.

that properly sample the configurations of the system, such as replica MC or parallel tempering.<sup>34</sup> Unfortunately, these algorithms lose their full efficiency because the coefficients in our Hamiltonian are temperature dependent. We thus use a simplified simulated annealing algorithm, which we expect to yield reasonable results at least for small disorder. The algorithm is the analog of the steepest-descent method used in the literature to minimize disordered GL functionals. We emphasize here that such minimization methods are often adequate when dealing with spin-glass-like systems as the free energy typically possesses many metastable minima. We first describe the microstructure obtained in the presence of long-range interactions. Figure 3(a) shows typical microstructures obtained in different regions of the phase diagram on a  $256 \times 256$  lattice, with the strength of the long-range term of  $A_1 = 4$ . These textures are fully consistent with what is observed in continuum GL theories and in experiments. In particular, we find the usual cross-hatched pattern for the tweed phase. Nevertheless, our RG approach provides a clear meaning to the

tweed phase, even in the absence of long-range interactions. We also show in Fig. 3(b) field-cooling and zero-field-cooling results that are usually used in both numerical studies and experiments to test for breaking of ergodicity and glassiness. These curves were obtained by averaging over  $10^3$  disordered configurations on  $64 \times 64$  lattices; other lattice sizes were tested without much difference. The curves shown in Fig. 3(b) may be interpreted as a signature of history dependence or ergodicity breaking. However, as argued previously, we do not expect the 2D version of the Hamiltonian (3) to have a spin-glass phase. The term “spin glass” should be understood here in the technical sense of the term; this does not prevent the system from showing kinematic “glassy behaviors” in the sense sometimes used by experimentalists. Therefore, our ZFC and FC results should be interpreted as a pure kinematic effect, possibly related to the slow convergence of our MC algorithm. Similar problems should occur when minimizing GL disordered functionals thanks to naive steepest-descent algorithms. It is worth emphasizing that probing spin-glass

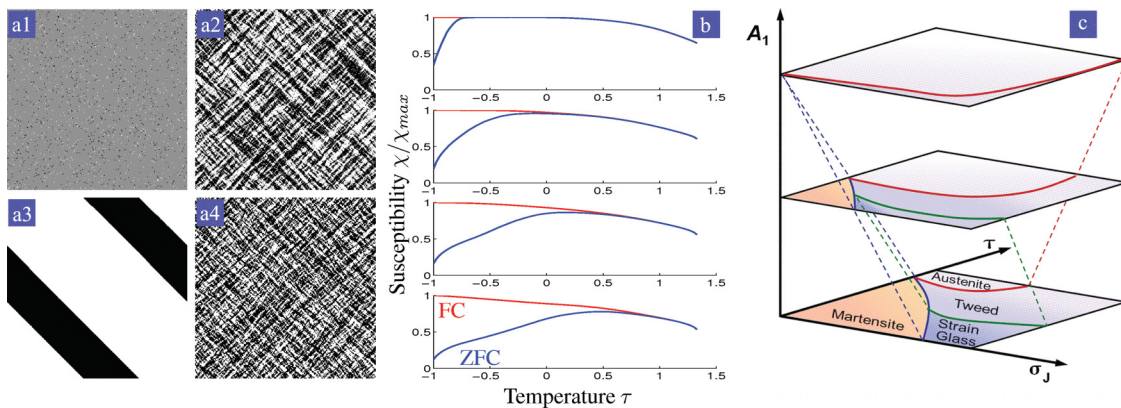


FIG. 3. (Color online) Monte Carlo results; the parameters are given in the text. (a) Typical microstructures obtained for  $A_1 = 4$  on a  $256 \times 256$  lattice in the different phases of the phase diagram. (a1) austenite, (a2) tweed, (a3) martensite, and (a4) strain glass. (b) Example of FC and ZFC curves with  $A_1 = 0$  for disorder  $\sigma_J = 1.5, 2, 2.25, 2.5$  from top to bottom. The curves represent the (normalized) susceptibility  $\chi = m/h$  against the temperature  $\tau$ . (c) Qualitative phase diagram showing the influence of the long-range interaction and disorder on the various phase transitions. Four different phases are shown: austenite, martensite, tweed, and strain glass.

phases in the usual spin models is a very subtle question to address numerically, and this cannot be answered using simple ZFC and FC experiments.

Finally, we suggest that the main features of our phase diagram persist even in the presence of long-range interactions (see related discussions in Refs. 23 and 24). The influence of the elastic long-range interaction on the austenite-tweed and tweed-strain-glass transition temperatures is shown schematically in Fig. 3(c). For no disorder ( $\sigma_J = 0$ ), the austenite-martensite transition temperature decreases linearly with  $A_1$ , as included phenomenologically within Landau theory. All the transition temperatures decrease with  $A_1$ ; in particular the glass transition is shifted to lower temperatures because the long-range interactions compete with the randomness.<sup>22</sup> In the asymptotic limit  $A_1 \rightarrow \infty$ , the disorder becomes irrelevant and only the austenite phase remains; we therefore conjecture that the phase diagram is shifted to lower temperatures with increasing  $A_1$ . This result could have implications in the study of colossal magnetoresistance materials where the interplay of disorder and long-range strain-mediated interactions has a bearing on the phase separation of coexisting insulating and conducting phases.<sup>35</sup>

### F. Extension to three dimensions

We now put our work focused on the 2D SR transition in a more general context and explain how one can extend the results to more realistic situations. Although our RG analysis is in 2D and is for a square-to-rectangle transition, we do not expect the salient features of the phase diagram to change for other transitions in 2D or 3D. As an example, let us discuss how one can extend our approach to the 3D cubic-to-tetragonal (CT) transition. A spin model for this transition was already proposed in Ref. 20. The CT transition is described in terms of a two-dimensional order parameter given by the adjunction of both deviatoric and shear distortions [ $e_2 = (\epsilon_{xx} - \epsilon_{yy})/\sqrt{2}$ ,  $e_3 = (\epsilon_{xx} + \epsilon_{yy} - 2\epsilon_{zz})/\sqrt{6}$ ]. The free energy functional can be written as a sum of three terms,  $F = \int d^3\vec{r} [f_L(e_2, e_3) + f_G(\vec{\nabla}e_2, \vec{\nabla}e_3) + \frac{A_1}{2}f_{LR}(e_2, e_3)]$ . The Ginzburg term reads  $f_G = \xi^2(|\nabla e_2|^2 + |\nabla e_3|^2)$ , whereas  $f_{LR}(e_2, e_3)$  is a long-range part that should not be important here (its explicit expression can be found in Ref. 20). The Landau part is slightly more complicated,  $f_L(e_2, e_3) = \tau(e_2^2 + e_3^2) - 2(e_3^3 - 3e_3e_2^2) + (e_2^2 + e_3^2)^2$ . This free energy can be minimized with respect to  $e_2$  and  $e_3$ , leading to four minima for  $\tau < \frac{9}{8}$ . Leaving out the  $e_2 = e_3 = 0$  minimum, the three others are given in the complex plane by  $\varepsilon(\tau)\omega_3^k$ , with  $\omega_3^3 = 1$ , and where similarly to the 2D case, one introduces

$$\varepsilon(\tau) = \frac{3}{4} \left( 1 + \sqrt{1 - \frac{8\tau}{9}} \right). \quad (9)$$

One can observe that  $\tau = 4/3$  now corresponds to the upper spinodal. Retaining the Landau minima in the free energy  $f_L$ , we define a pseudospin  $\vec{S}$  such that  $\vec{e} = (e_2, e_3)^T \rightarrow \varepsilon(\tau)\vec{S}$ , with

$$\vec{S} \in \left\{ \begin{pmatrix} 0 \\ 0 \end{pmatrix}, \begin{pmatrix} 1 \\ 0 \end{pmatrix}, \begin{pmatrix} -1/2 \\ \pm\sqrt{3}/2 \end{pmatrix} \right\}. \quad (10)$$

The Landau part of the free energy hence reduces to  $f_L(\tau) = \varepsilon^2(\tau)g_L(\tau)\vec{S}^2(\vec{r})$ , where  $g_L(\tau) = \tau - 1 + [\varepsilon^2(\tau) - 1]^2$ . This leads to the pseudospin model

$$\beta H = -J(\tau) \sum_{\langle i,j \rangle} \vec{S}_i \cdot \vec{S}_j + \Delta(\tau) \sum_i \vec{S}_i^2 + \frac{\beta A_1}{2} \sum_{ij} U_{ij} \vec{S}_i \cdot \vec{S}_j, \quad (11)$$

with  $\Delta(\tau) = \frac{D_0(\tau)}{2}[g_L(\tau) + 6\xi^2]$ ,  $J(\tau) = D_0(\tau)\xi^2$ , and  $D_0(\tau)$  defined as before. This model is a three-dimensional clock model with long-range interactions. The two-dimensional spin  $\vec{S}$  can take three values on the unit circle in addition to the value  $\vec{S} = \vec{0}$ .

It is straightforward to extend the renormalization group method to this class of models. This is done by considering hierarchical lattices with fractal dimension close to 3, for which the RG decimation step becomes exact if one introduces an additional coupling  $-K \sum_{\langle i,j \rangle} (\vec{S}_i \cdot \vec{S}_j)^2$ . We solved exactly the pure model defined by Eq. (11) for  $A_1 = 0$ , on a three-dimensional hierarchical lattice, to find two phases separated by a first-order phase transition around  $\tau \simeq 1$ , as expected. The high-temperature austenite phase is characterized by  $\langle \vec{S} \rangle = \vec{0}$ , whereas the martensite phase shows one of the three variants lying on the circle  $|\vec{S}| = 1$ . Quench disorder can be easily introduced through random  $J_{ij}$  couplings and the RG iteration can be generalized to the disordered case. The calculated phase diagram is very similar to that obtained for the SR transition in 2D in Fig. 2(a), although the numerical resolution of the RG equations is much more difficult in this case. We find two different “paraelastic” phases, the usual austenite characterized by the RG fixed point ( $J^* = 0$ ,  $\Delta^* = \infty$ ), and a tweed fixed point with ( $J^* = 0$ ,  $\Delta^* = -\infty$ ) which corresponds to a disordered phase of martensitic variants. We also expect this kind of model to show a spin- or strain-glass phase, at least in high dimensions. These results are consistent with our extensive study of the SR 2D model. It is thus very tempting to conjecture that the behavior of even more complicated clock models, describing more evolved transitions, should have a phase diagram very similar to that of the SR model.

### IV. EXPERIMENTAL PHASE DIAGRAM

To check the predictions of our RG calculations, we experimentally investigated the phase transformation behavior as a function of temperature  $T$  and concentration  $x$  for  $\text{Ti}_{50}(\text{Pd}_{50-x}\text{Cr}_x)$  alloys.

In the low-Cr-content regime ( $x \leq 8$ ), the system undergoes a  $B2 \rightarrow B19$  martensitic transformation. The transformation properties of  $\text{Ti}_{50}(\text{Pd}_{45}\text{Cr}_5)$  alloy are shown in Figs. 4(a1)–4(a3). The  $B2 \rightarrow B19$  martensitic transformation at its transformation temperature  $M_s$  is accompanied by a sharp increase in electrical resistivity [Fig. 4(a1)]. It is found that the electrical-resistivity curve deviates from linearity above  $M_s$ , and the onset temperature of the deviation  $T_{nd}$  is defined as the tweed formation temperature. The martensitic transformation is also characterized by a frequency-independent peak in internal friction [Fig. 4(a2)] and a frequency-independent



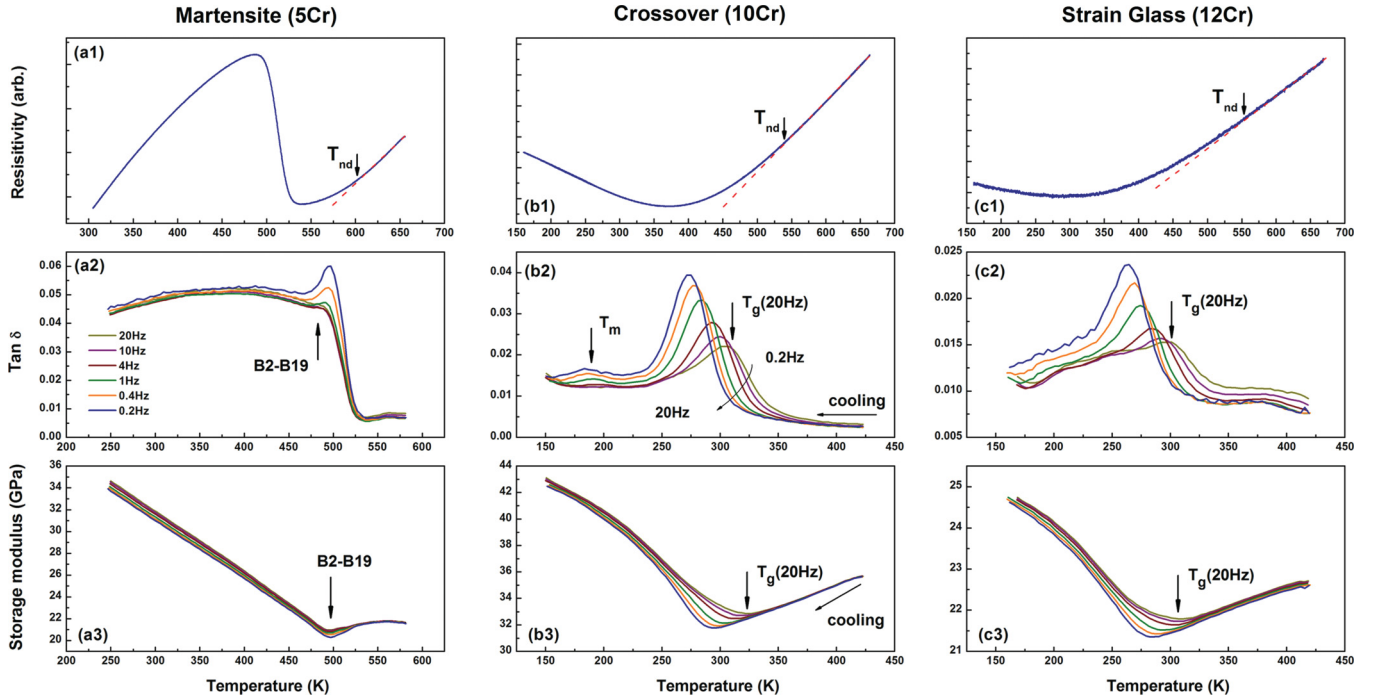


FIG. 4. (Color online) The transformation behavior of  $\text{Ti}_{50}\text{Pd}_{(50-x)}\text{Cr}_x$  alloys as a function of Cr (point defect) concentration, by means of electrical resistivity and DMA measurements. (a1), (a2), (a3) show that the low-Cr-content  $\text{Ti}_{50}(\text{Pd}_{45}\text{Cr}_5)$  alloy undergoes a normal martensitic transformation, whereas (c1), (c2), (c3) show that the high-Cr-content  $\text{Ti}_{50}(\text{Pd}_{38}\text{Cr}_{12})$  alloy undergoes a strain-glass transition. (b1), (b2), (b3) show that the intermediate-Cr-content  $\text{Ti}_{50}(\text{Pd}_{40}\text{Cr}_{10})$  alloy, located in the crossover region between martensite and strain glass, transforms from the parent phase to strain glass (at  $T_g$ ) and then to martensite (at  $T_m$ ).

dip in storage modulus [Fig. 4(a3)]. Note that the frequency independence in the dynamical mechanical analysis dip and peak is an important feature of martensitic transformation.

For high Cr content ( $x \geq 12$ ), the alloys adopt a transition path from austenite through tweed to strain glass. The transformation properties of  $\text{Ti}_{50}(\text{Pd}_{38}\text{Cr}_{12})$  alloy are shown in Figs. 4(c1)–4(c3). As shown in Fig. 4(c1), the electrical resistivity also shows a deviation from linearity below  $T_{nd}$ , indicating the appearance of a tweed state. The alloy undergoes a frequency-dependent storage modulus dip and an internal friction peak [Figs. 4(c2) and 4(c3)], in contrast with the frequency-independent behaviors during the martensitic transformation [Fig. 4(a1)]. This demonstrates that a dynamic freezing strain-glass transition occurs in high-Cr-content alloys. The ideal glass frozen temperature ( $T_0$ ) was obtained by fitting the DMA dip temperature  $T_g(\omega)$  and frequency  $\omega$  with the Vogel-Fulcher relation  $\omega = \omega_0 \exp\{-E_a/k_B[T_g(\omega) - T_0]\}$ . Note that the frequency dependence in the DMA dip and peak is an important feature of strain-glass transformation.

For the crossover regime ( $9 < x < 12$ ) between martensite and strain glass, the alloys experience all four strain states upon cooling, and a spontaneous transformation from strain glass to the martensite phase (9R) takes place. Figures 4(b1)–4(b3) show the predicted spontaneous transformation behavior for the  $\text{Ti}_{50}(\text{Pd}_{40}\text{Cr}_{10})$  alloy. Upon cooling, the tweed phase first forms at  $T_{nd} = 531$  K [Fig. 4(b1)]. Further cooling gives rise to a frequency-dispersive internal friction peak and a storage modulus dip in the DMA results in Figs. 4(b2) and 4(b3), which correspond to a strain-glass transition with frozen temperature  $T_0$  of 250 K. With a further decrease in

temperature, a frequency-independent internal friction peak appears in the DMA results [Fig. 4(b2)], which shows a

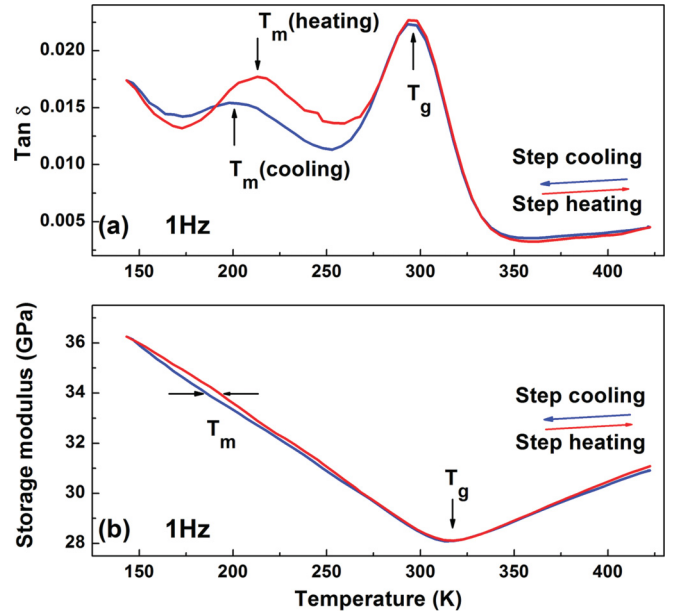


FIG. 5. (Color online) (a) Internal friction and (b) storage modulus for  $\text{Ti}_{50}(\text{Pd}_{40}\text{Cr}_{10})$  alloy during step cooling and step heating processes, under an ac stress field with a frequency of 1 Hz. The nearly zero thermal hysteresis of the higher-temperature transition at  $T_g$  suggests that it is a glass transition, whereas the large thermal hysteresis (about 10 K) of the lower-temperature transition (at  $T_m$ ) suggests that it is a first-order phase transformation.

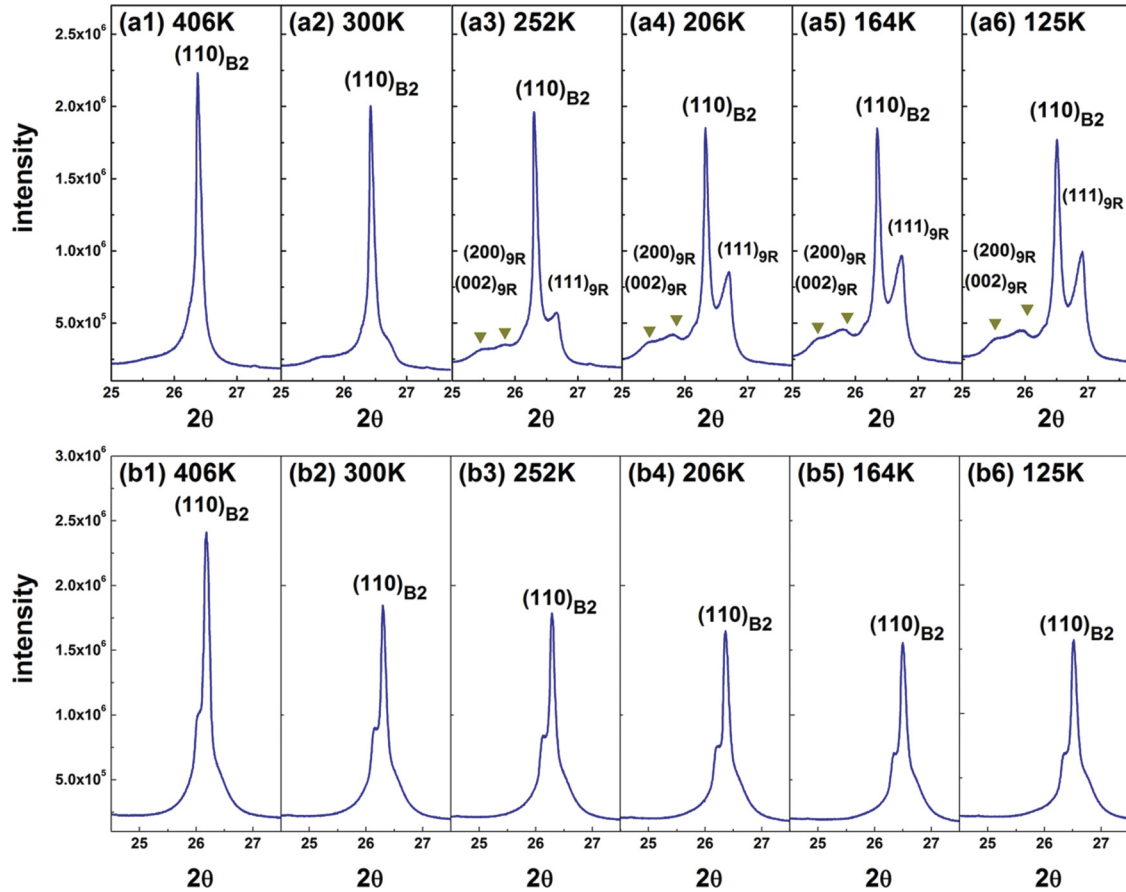


FIG. 6. (Color online) *In situ* synchrotron XRD patterns of (a)  $\text{Ti}_{50}(\text{Pd}_{40}\text{Cr}_{10})$  alloy and (b)  $\text{Ti}_{50}(\text{Pd}_{38}\text{Cr}_{12})$  alloy from 400 to 125 K. Obvious peak splitting with decreasing temperature can be found in the  $\text{Ti}_{50}(\text{Pd}_{40}\text{Cr}_{10})$  alloy, corresponding to the first-order transition shown in Fig. 5. However, no such splitting occurs in the strain-glass alloy  $\text{Ti}_{50}(\text{Pd}_{38}\text{Cr}_{12})$ .

similar feature to the martensitic transformation [Fig. 4(a2)]. This indicates that a certain phase transformation occurs. We further studied the thermal hysteresis of the two phase transformations to characterize them. As shown in Fig. 5, the glass transition at higher temperature is associated with nearly zero thermal hysteresis in the internal friction anomaly and storage modulus, which is consistent with previous studies on the strain-glass transition.<sup>11–15</sup> From the peak intervals of the internal friction and storage modulus in Fig. 5, we found that the lower-temperature transition is associated with a thermal hysteresis of about 10 K, which suggests a first-order transition. We interpret the transition as a spontaneous transformation from strain glass to normal martensite. We also employed *in situ* synchrotron x-ray diffraction (XRD) to check the predicted spontaneous behavior for  $\text{Ti}_{50}(\text{Pd}_{40}\text{Cr}_{10})$ , as shown in Fig. 6(a). In the tweed region (400 and 300 K), only a sharp  $(110)_{B2}$  peak appears without peak splitting. At 252 K where the strain glass is frozen, clear peak splitting can be observed, and the new peaks can be indexed as  $(002)_{9R}$ ,  $(200)_{9R}$ , and  $(111)_{9R}$ , suggesting the presence of short-range order associated with the 9R structure. With further decrease to 125 K, the peak splitting becomes stronger and the 9R peak height drastically increases, indicating the formation of 9R martensite. To exclude the possibility that the above peak splitting is caused by nanodomain growth, contrast *in situ* synchrotron XRD was also carried out on

$\text{Ti}_{50}(\text{Pd}_{38}\text{Cr}_{12})$ , in which the strain-glass state is stable, but that system can also show nanodomain growth with decrease of temperature.<sup>11–13</sup> Figure 6(b) clearly shows that the  $(110)_{B2}$  peak shows no splitting throughout the measurement temperature range. Therefore, the peak splitting in the  $\text{Ti}_{50}(\text{Pd}_{40}\text{Cr}_{10})$  alloy should indicate a transformation from strain glass to martensite.

The microstructure evolution in  $\text{Ti}_{50}(\text{Pd}_{40}\text{Cr}_{10})$  was further investigated by *in situ* TEM observations from 330 to 110 K, and the results are shown in Fig. 7. In the tweed region (330 and 300 K), contrast from nanodomains can be seen with diffused superspots in the diffraction pattern; however, when the sample is cooled to 110 K (the martensite region), where 9R peaks appear in the Bragg reflections, parallel martensite domains are visible in addition to nanodomains. From the present experimental results, we conclude that the second-step transition is a spontaneous transition from a strain-glass to the normal martensite phase 9R. We note that although the spontaneous transition does occur, the parent peak still exists in the synchrotron XRD pattern. This suggests that not all the nanodomains in the strain glass spontaneously transform into 9R martensite within our measurement window. The lack of completeness of this spontaneous transition can be ascribed to kinetic limitations. In addition, it is also noted that the spontaneous phase transition here is rather weak and sluggish, as the phase mixture of strain glass and martensite exists

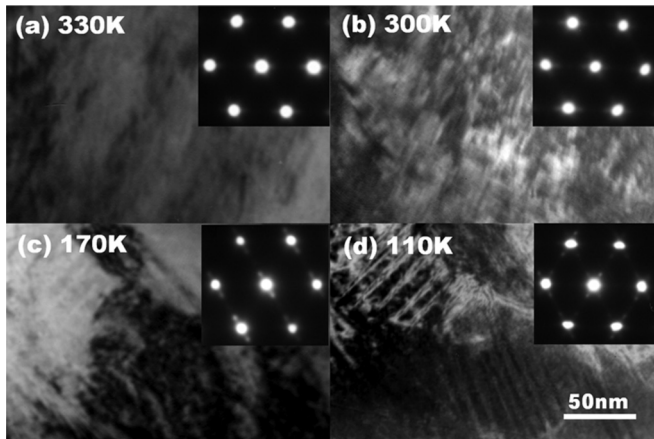


FIG. 7. (Color online) *In situ* TEM observation of  $\text{Ti}_{50}(\text{Pd}_{40}\text{Cr}_{10})$  alloy from 330 to 110 K. Upon cooling, the nanodomains in the tweed region (330 and 300 K) gradually transform to parallel martensitic domains (170 and 110 K). The corresponding diffraction spots from newly formed martensite domains become stronger with decreasing temperature. This suggests a spontaneous transition from strain glass to martensite, consistent with the DMA results shown in Fig. 5 and the *in situ* synchrotron XRD patterns shown in Fig. 6(a).

over a wide temperature range. This could be the reason for the absence of anomaly in our conventional differential scanning calorimetry measurements (in which only latent heat is measured). Changes in heat capacity may aid in identifying the spontaneous transition.

According to the above experimental results, a modification is made to the previous phase diagram of  $\text{Ti}_{50}(\text{Pd}_{50-x}\text{Cr}_x)$  alloys,<sup>36</sup> where a crossover composition regime is included, as shown in Fig. 2. A similar phase diagram, including the spontaneous phase transition, can be found in the  $\text{Ti}_{50}(\text{Ni}_{50-x}\text{Fe}_x)$  strain-glass alloy,<sup>37</sup> and also in the La-modified  $\text{Pb}(\text{Zr}_{0.65}\text{Ti}_{0.35})\text{O}_3$  ferroelectric relaxor ceramic.<sup>38</sup>

## V. CONCLUSION

Our study emphasizes the importance of statistical mechanics and spin-glass theory which, in conjunction with experiments, provide a general framework to understand universal features of the strain-glass and tweed phases in ferroelastic materials. Our specific aim has been to emphasize how pseudospin models of martensites provide a predictive route towards understanding aspects of glass behavior seen in experiments. This suggests that ferroelastics are very similar to ferroelectric and ferromagnetic materials, in the sense that they can be described within the same framework of statistical

mechanics of spin models. A crucial feature of ferroelastic spin models is the additional  $S = 0$  state, which allows for two different “paraelastic” phases, austenite and tweed. Tweed is characterized in our study as a disordered phase of martensitic variants. This tends to show that the tweed state observed is a true thermodynamical phase, that exists even in the absence of long-range interactions, just like martensite and austenite. This is an important outcome of our study as so far tweed has been mostly interpreted as a spin glass or as a static precursor. We also believe that many key ideas emanating from the spin-glass and statistical mechanics community should apply to the case of ferroelastics as well. For example, it still seems widely believed in the strain-glass community that the precise form of the quenched disorder modeling impurities is crucial for an understanding of the physics of the systems under scrutiny. We know from experience that this is not true for spin glasses, and it seems highly unlikely that it could be true for disordered ferroelastics. We also wish to emphasize that long-range interactions, although crucial for microstructures, do not seem to be relevant to understand the global topology of the phase diagram.

Although we have mainly focused on a specific model in 2D, we argued in Sec. III F that our conclusions should apply to a wide variety of 2D and 3D ferroelastic transitions; in particular, we believe that our calculated phase diagram is “generic.” To be more precise, we expect to find very similar topology of phase diagrams for other transitions with more variants in both two and three spatial dimensions. The alloy we chose as an example in the paper gives rise to two product phases as a function of disorder ( $B2$  to  $B19$ , and  $B2$  to  $9R$ ). Our analysis predicts that ferroelastics undergoing transitions to one product phase, such as  $\text{TiNiFe}$ ,  $\text{FePd}$ , or  $\text{CaTiO}_3$ , will show a very similar phase diagram and a spontaneous transition. We thus expect the general topology of the phase diagram shown in Fig. 3(c) to be quite robust.

## ACKNOWLEDGMENTS

We thank Gao Jinghui and Zhang Zhen for help with the experiments. D.X. and X.R. are grateful to Spring-8 for the use of beamline BL15XU where the synchrotron XRD measurements were made. We thank A. Lazarescu and D. Sherrington for stimulating discussions. R.V. and X.D. are grateful to the Theoretical Division and CNLS, LANL, for support. This work was supported by the US DOE at LANL (Grant No. DE-AC52-06NA25396) as well as the NSFC of China (Grants No. 51171140 and No. 51231008), the 973 Project of China under Grant No. 2010CB631003, and the 111 Project of China.

\*dingxdxjtu@gmail.com

†txl@lanl.gov

<sup>1</sup>K. H. Eckelmeyer, *Scr. Metall.* **10**, 667 (1976).

<sup>2</sup>S. Miyazaki, K. Otsuka, and Y. Suzuki, *Scr. Metall.* **15**, 287 (1981).

<sup>3</sup>K. N. Melton and O. Mercier, *Acta Metall.* **29**, 393 (1981).

<sup>4</sup>S. Miyazaki and K. Otsuka, *Metall. Mater. Trans. A* **17**, 53 (1986).

<sup>5</sup>W. Tang, *Metall. Mater. Trans. A* **28**, 537 (1997).

<sup>6</sup>C. Somsen, H. Zähres, J. Kästner *et al.*, *Mater. Sci. Eng. A* **273–275**, 310 (1999).

<sup>7</sup>K. Otsuka and X. Ren, *Prog. Mater. Sci.* **50**, 511 (2005).

<sup>8</sup>D. Sherrington, *J. Phys.: Condens. Matter* **20**, 304213 (2008).

<sup>9</sup>S. Kartha, T. Cast'an, J. A. Krumhansl, and J. P. Sethna, *Phys. Rev. Lett.* **67**, 3630 (1991).



- <sup>10</sup>S. Semenovskaya and A. G. Khachaturyan, *Acta Mater.* **45**, 4367 (1997).
- <sup>11</sup>S. Sarkar, X. Ren, and K. Otsuka, *Phys. Rev. Lett.* **95**, 205702 (2005).
- <sup>12</sup>X. Ren *et al.*, *Philos. Mag.* **90**, 141 (2010).
- <sup>13</sup>D. Wang, Y. Wang, Z. Zhang, and X. Ren, *Phys. Rev. Lett.* **105**, 205702 (2010).
- <sup>14</sup>Y. Zhou *et al.*, *Acta Mater.* **58**, 5433 (2010).
- <sup>15</sup>Y. Wang, X. Ren, and K. Otsuka, *Phys. Rev. Lett.* **97**, 225703 (2006).
- <sup>16</sup>J. A. De Toro, M. A. L. de la Torre, M. A. Arranz, J. M. Riveiro, and J. L. Martinez, *J. Appl. Phys.* **87**, 6534 (2000).
- <sup>17</sup>J. P. Sethna, *Statistical Mechanics: Entropy, Order Parameters, and Complexity* (Oxford University Press, New York, 2006).
- <sup>18</sup>D. Sherrington, *Disorder and Strain-Induced Complexity in Functional Materials*, Springer Series in Materials Science, Vol. 148 (Springer, Berlin, 2012), pp. 177–199.
- <sup>19</sup>S. R. Shenoy and T. Lookman, *Phys. Rev. B* **78**, 144103 (2008).
- <sup>20</sup>R. Vasseur, T. Lookman, and S. R. Shenoy, *Phys. Rev. B* **82**, 094118 (2010).
- <sup>21</sup>M. Blume, *Phys. Rev.* **141**, 517 (1966); H. W. Capel, *Physica (Amsterdam)* **32**, 966 (1966); M. Blume, V. J. Emery, and R. B. Griffiths, *Phys. Rev. A* **4**, 1071 (1971).
- <sup>22</sup>R. Vasseur and T. Lookman, *Phys. Rev. B* **81**, 094107 (2010).
- <sup>23</sup>P. Lloveras, T. Castán, M. Porta, A. Planes, and A. Saxena, *Phys. Rev. Lett.* **100**, 165707 (2008).
- <sup>24</sup>P. Lloveras, T. Castán, M. Porta, A. Planes, and A. Saxena, *Phys. Rev. B* **80**, 054107 (2009).
- <sup>25</sup>S. F. Edwards and P. W. Anderson, *J. Phys. F* **5**, 965 (1975).
- <sup>26</sup>D. Sherrington and S. Kirkpatrick, *Phys. Rev. Lett.* **35**, 1792 (1975).
- <sup>27</sup>M. Mezard, G. Parisi, and M. A. Virasoro, *Spin Glass Theory and Beyond* (World Scientific, Singapore, 1987).
- <sup>28</sup>A. N. Berker and M. Wortis, *Phys. Rev. B* **14**, 4946 (1976).
- <sup>29</sup>N. S. Branco and B. M. Boechat, *Phys. Rev. B* **56**, 11673 (1997).
- <sup>30</sup>S. K. Ghatak and D. Sherrington, *J. Phys. C* **12**, 3149 (1977).
- <sup>31</sup>V. O. Özçelik and A. N. Berker, *Phys. Rev. E* **78**, 031104 (2008).
- <sup>32</sup>J. Snyder, J. S. Slusky, R. J. Cava, and P. Schiffer, *Nature (London)* **413**, 48 (2001).
- <sup>33</sup>T. Lookman, S. R. Shenoy, K. Ø. Rasmussen, A. Saxena, and A. R. Bishop, *Phys. Rev. B* **67**, 024114 (2003).
- <sup>34</sup>R. H. Swendsen and J.-S. Wang, *Phys. Rev. Lett.* **57**, 2607 (1986).
- <sup>35</sup>K. Ahn, T. Lookman, and A. R. Bishop, *Nature (London)* **428**, 401 (2004).
- <sup>36</sup>Y. Zhou *et al.*, *Appl. Phys. Lett.* **95**, 151906 (2009).
- <sup>37</sup>J. Zhang, Y. Wang, X. Ding *et al.*, *Phys. Rev. B* **84**, 214201 (2011).
- <sup>38</sup>H. Liu, R. Harrison, and A. Putnis, *J. Appl. Phys.* **90**, 6321 (2001).